Spectrochimica Acta Part B: Atomic Spectroscopy 233 (2025) 107305

Contents lists available at ScienceDirect

Spectrochimica Acta Part B: Atomic Spectroscopy

journal homepage: www.elsevier.com/locate/sab

Enhancing laser ablation inductively coupled plasma mass spectrometry analysis through empirical modeling of crater geometry

Antea Hrepić [a,b], Filip Cernatič [a], Kristina Mervič [c], Sanda Rončević [d], Ivan Nemet [d], Martin Šala [a,*]

[a] Department of Analytical Chemistry, National Institute of Chemistry, Hajdrihova 19, 1000 Ljubljana, Slovenia
[b] Faculty of Chemistry and Chemical Technology, University of Ljubljana, Večna pot 113, 1000 Ljubljana, Slovenia
[c] Department of Catalysis and Chemical Reaction Engineering, National Institute of Chemistry, Hajdrihova 19, 1000 Ljubljana, Slovenia
[d] Department of Chemistry, Faculty of Science, University of Zagreb, Horvatovac 102a, 10000 Zagreb, Croatia

ARTICLE INFO

Keywords:
LA-ICP-MS
Mapping
Crater geometry
Modeling
Laser wavelength

ABSTRACT

Laser ablation inductively coupled plasma mass spectrometry (LA-ICP-MS) systems are engineered to produce uniform, flat-top beam profiles for optimal surface sampling. In practice, however, rounder beam profiles are prevalent. Their geometrical characteristics can be mathematically described using the two-dimensional super-Gaussian or even a Gaussian function for smaller beam sizes, with the super-Gaussian factor (n) serving as a quantifier. Since the beam profile and the ablation grid have a direct influence on the amount of sampled surface material, the idea is to reduce the ablation grid by sub-pixel mapping to improve the accuracy of surface scanning, increase pixel density, improve spatial resolution, and increase signal-to-noise ratio (SNR). This paper explores the relationship between super-Gaussian order (n), beam size, and laser fluence for circular beams, using two laser ablation systems with different wavelengths – 193 nm and 213 nm nanosecond lasers. An empirical model was developed to yield the factor n, facilitating the determination of the contraction factor (k). Identifying the precise contraction factor for each beam size brings the beam profile closer to a flat-top shape, producing smoother post-ablation surfaces and enhancing image quality due to heightened pixel density. Ultimately, such models improve our understanding of crater geometry optimization, leading to better analytical outcomes in LA-ICP-MS analysis.

1. Introduction

In recent years, laser ablation inductively coupled plasma mass spectrometry (LA-ICP-MS) has gained recognition as a powerful, high-resolution imaging method that has attracted attention from various fields such as biology [1], biomedicine [2], forensics [3], and geology [4].

Since its introduction [5], the core principle of LA-ICP-MS has remained unchanged, with its performance being influenced by laser parameters, ablation cell design, aerosol transport mechanisms, and ICP-MS operating conditions. Lasers can be categorized according to different aspects, such as the pulse duration, and the wavelength of the emitted energy [6]. Two interesting laser categories in LA-ICP-MS according to the pulse duration are nanosecond (ns) and femtosecond (fs) lasers. Because the pulse width of the fs laser is shorter (10^{-15} s) than the electron-lattice heating, laser-matter interaction in femtosecond lasers is essentially athermal, with no interaction between the incipient laser ablation-generated plume and the laser beam itself [7,8]. In contrast, nanosecond laser-matter interactions are probabilistic, relying on existing lattice defects, high laser fluence, and longer pulse duration (10^{-9} s), which leads to melting as the dominant process and results in fractionation [9,10]. Consequently, craters produced using two different ablation systems show distinct differences in their surface morphology. Femtosecond laser ablation generates smoother and more uniform craters with well-defined brims that show no melting and re-deposited droplets of melted matter. The short pulse duration prevents thermal effects, eliminating melt formation and material re-deposition. In contrast, due to the extended pulse duration, nanosecond laser ablation produces craters with notable thermal artifacts. The molten material often re-solidifies both within and around the crater, creating irregular surface features and ejected droplets that re-deposit on the crater walls, ultimately yielding less precise and more textured crater formations

* Corresponding author.
E-mail address: martin.sala@ki.si (M. Šala).

https://doi.org/10.1016/j.sab.2025.107305
Received 25 April 2025; Received in revised form 14 July 2025; Accepted 22 August 2025
Available online 27 August 2025

[11–13].

However, femtosecond lasers are quite costly and some studies [14,15] even suggested that their performance is not as superior to nanosecond lasers on certain isotopic analyses [16]. As a result, despite some drawbacks compared to the fs lasers, ns laser ablation ICP-MS remains a highly reliable and widely used method for elemental and isotopic analysis [9].

LA-ICP-MS systems operating at different wavelengths exhibit distinct characteristics that influence their analytical performance. Many studies [17–20] demonstrate that shorter wavelengths are more suitable because of the reduced fractionation effects. Among the available laser wavelengths, the 193 nm and 213 nm nanosecond lasers have emerged as the most frequently utilized ones. The 193 nm laser system, an ArF excimer laser, demonstrates superior performance in terms of spatial resolution and is particularly effective when analyzing silicate materials [6,21]. This shorter wavelength consistently produces smaller particles, predominantly below 150 nm, resulting in a more stable transient signal and smaller variations of intensity ratios. Small particle sizes also allow for a more efficient conversion of particles into ions, resulting in higher sensitivity per ablated volume. The signal for the 193 nm laser also shows better matrix independence, which could be due to the larger photon energy or the shallow optical depth [22]. The 213 nm laser, derived from frequency quintupling the emitted light of an Nd:YAG solid-state laser, has been described as a good alternative for the 193 nm laser [23,24]. It produces larger particles in comparison, with an upper size limit of 500 nm [22]. The 213 nm wavelength typically causes less surface damage to samples and operates with good stability. For some materials, it even provided better depth resolution [21,22]. Both laser systems have become fundamental research tools in environmental studies [25], geology [26], and materials science [27].

In recent years, there has been significant progress in the development of rapid response laser ablation cells and sample transport technologies, like the aerosol rapid introduction system (ARIS) [28]. These systems are designed to minimize aerosol dispersion in the cell and to greatly reduce washout time. When the aerosol exits the cell, it must be efficiently transported to the ICP-MS [29], which has been achieved by reducing the diameter of the transport tubing and eliminating dead volumes in the injector [30]. While these modifications help minimize aerosol dispersion, they also reduce the mass flux outflow from the cell. If the density of ablated particles exceeds the capacity of the transport tubing, excess material may be lost through gravitational sedimentation or inertial deposition, reducing efficiency [29]. Aimed to balance the need for rapid and efficient analysis with the physical limitations of aerosol transport, these advancements have significantly accelerated mapping times [29], increasing the mapping speed from 2 to 10 to 200–1000 kpixels per hour [31]. Such acquisition rates combined with sensitive ICP-MS instrumentation facilitate the sampling of large surface areas with small laser beam sizes [32,33]. However, sensitivity issues can play a role when using small beam sizes due to the reduction of ablated material [34].

Typically, the laser beam profiles in LA-ICP-MS instruments are homogenized to produce a flat-top beam profile that minimizes surface degradation from excessive heating [35]. In practice, these profiles often resemble a super-Gaussian, approaching a Gaussian profile at small laser beam sizes (<5 μm) [34,36]. The geometrical profile of the crater can be quantified using the parameter n, which describes the super-Gaussian order. It is essentially a mathematical description of a super-Gaussian beam profile, a shape parameter that gauges how closely the beam resembles an ideal flat-top, indicating the degree of central fitness and edge steepness in a single number. The smaller the n, the more Gaussian the shape. This underscores the critical importance of the beam profile for surface sampling, as ablation on a conventional single-pulse ablation grid may result in unrealistic sampling and undersampling of the surface [34,37], as depicted in Fig. 1. It shows post-ablation surfaces after mapping with the conventional single-pulse mode, using a single laser shot (dosage, $D = 1$).

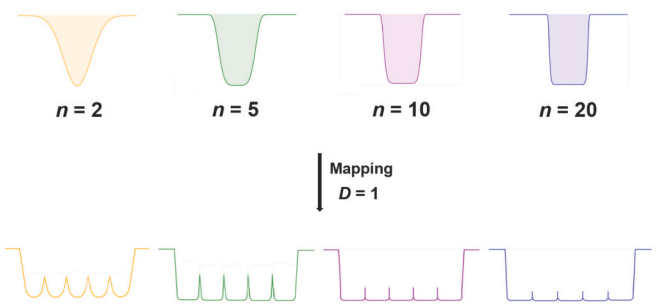

Fig. 1. Different super-Gaussian orders (n) and an illustration of the post-ablation surface using the shot number per pixel, dosage, $D = 1$. At the value of $n = 2$, the crater follows a Gaussian behavior, while at higher values resembles a super-Gaussian, approaching a flat-top shape when the super-Gaussian order → ∞.

To address these challenges, the oversampling approach has proven successful [29,33,34,36]. The method involves contracting the ablation grid, increasing the density of laser spots by overlapping them, thereby generating more pixels mapped in the same area. To reduce sensitivity issues in LA-ICP-MS, "thick" samples are used to accumulate counts of multiple partially overlapping laser shots (dosage) to generate a single pixel [34]. This ensures a smoother post-ablation surface, an enhanced signal-to-noise ratio (SNR), and improved lateral resolution as well as layer-by-layer mapping [36]. A high dosage is needed to maintain an SNR as high as possible. On the other hand, a high dosage increases the degree of blurring. While this approach can result in more accurate surface sampling and improved image quality, it is important to find a balance between image noise and image blur [32]. Noise is directly related to the counting statistics in ICP-MS, and blur arises mostly during laser ablation sampling, where a near-infinite continuous analog signal is converted into discrete, finite-sized pixels [34].

The contraction approach is commonly used in dentistry [38], industrial micromachining [39], laser vision correction [40], and other applications to achieve high-quality surface finishes. These applications usually use laser devices with a Gaussian beam profile and optimized laser ablation conditions derived from geometrical modeling [41,42]. That kind of approach uses spot-related three-dimensional laser ablation crater geometries, allowing for the correlation between the area illuminated by the beam, surface topography, and the induced roughness [36,40,42].

While modeling has been successful in the optimization of the LA-ICP-MS parameters, including beam size, repetition rate, scanning speed, dwell time, and acquisition time [34,36], experimental data needs to be collected in order to gain accurate information for such an approach. For that reason, this paper focuses on exploring the relationship between super-Gaussian order (n), beam size (BS), and laser fluence (F) for round beams, comparing data utilizing two laser ablation systems with different wavelengths, 193 nm and 213 nm nanosecond lasers. An empirical model was devised, generating the factor n, and, thus, facilitating the determination of the accurate contraction factor (k). Identifying the precise contraction factor for each beam size and n will result in smoother post-ablation surfaces and improved image quality due to heightened pixel density. Such models will deepen comprehension of crater geometry optimization, ultimately enhancing analytical outcomes in LA-ICP-MS analysis.

2. Materials and methods

2.1. Sample preparation

The gelatin standards were prepared according to the earlier established protocol [43], using porcine-skin gelatine (type A, bloom strength 300), purchased from Sigma-Aldrich.

Gelatin was used as a standard because of its diversity. Its structure resembles organic tissue samples, it demonstrates good temporal stability, has a low ablation threshold, and a more homogeneous distribution of elements can be achieved, avoiding the "coffee-stain" effect, where the edges of a dried droplet have a higher concentration of material compared to the center. It can also be easily prepared with specific elements, allowing the concentration range to be tailored to the analysis needs, making it more versatile than the existing NIST SRM 610 and 612 glass standards [43]. Preliminary tests also showed more defined craters, compared to those of NIST standards, using the same parameters that were explored in our research.

2.2. LA-ICP-MS measurements

Dried gelatin samples were subjected to laser ablation to create round ablation craters using a range of beam diameters. Two different ablation systems were used:

(i) A 193 nm ArF* (Analyte G2, Teledyne Photon Machines Inc., Bozeman, MT), was equipped with a standard two-volume ablation cell (HelEx II, aerosol washout time of approximately 0.5 s) and a helium carrier flow rate of 0.3 and 0.5 L min^{-1} for cup and cell, respectively. Different beam sizes were used to create 5 μm, 10 μm, 15 μm, 20 μm, and 25 μm ablation craters. The experiments were carried out at the National Institute of Chemistry (NIC) in Ljubljana, Slovenia.

(ii) A 213 nm (Analyte G2, Teledyne Photon Machines Inc., Bozeman, MT), was also equipped with a HelEx II ablation cell designed to provide efficient and uniform sample ablation. The ablation craters produced were 10 μm, 15 μm, 20 μm, and 25 μm in diameter. The measurements were performed at the Faculty of Science (PMF) in Zagreb, Croatia.

The measurements were carried out utilizing laser fluences of 0.5 J cm^{-2}, 1.0 J cm^{-2}, 2.0 J cm^{-2}, 3.0 J cm^{-2}, and 4.0 J cm^{-2}. For each combination of beam size and fluence, 25 replicate measurements were conducted to ensure statistical reliability.

2.3. Optical profilometry measurements

The morphologies of the craters were examined using optical profilometry (Zegage PRO HR, Zygo Corporation, CT), and representative surface profiles are provided in Supplementary Material, SI-1. They were used as an input for retrieving the volume of the craters and the super-Gaussian order (n) through geometrical modeling. 3D information was recorded using a 50× magnification lens, yielding a lateral resolution of 0.173 μm (equivalent to the step size) and surface topography repeatability better than 3.5 nm.

2.4. Software and modeling

The numerical calculations and simulation modeling were performed using Python 3.11. A custom-developed internal script was utilized to fit a super-Gaussian function to the crater profiles obtained from a profilometer (the script is available upon request). The profilometer provides high-resolution measurements of the surface topography, which are crucial for accurately modeling the laser ablation craters. The process of determining the laser ablation crater profiles was as follows:

- Selection of the region of interest
- Fitting of background surface
- Background surface subtraction
- Super-Gaussian function fitting (initial fit, intermediate fit, and final fit)
- Determination of super-Gaussian order (n), the volume of the crater, and the coefficient of determination (R^2).

A more detailed description can be found in Supplementary Material, SI-2.

3. Results and discussion

The morphology of laser ablation craters exhibits more complexity than a simple flat-top profile. Their geometric characteristics can be mathematically represented by symmetric probability density functions with elevated super-Gaussian orders (n), with smaller beam diameters trending toward Gaussian profiles. The specific crater geometry is intrinsically linked to both the material's optical characteristics and its interaction with the incident laser wavelength [34,36].

While laser ablation systems are engineered to deliver homogenized, flat-top beam profiles for optimal surface sampling, round beam profiles remain predominant in LA-ICP-MS applications in the small beam size range. This prevalence stems from their widespread commercial availability and a fundamental physical observation that even square beam profiles naturally tend to assume a rounded shape when beam sizes are reduced [34].

Super-Gaussian beam profiles for round (○) beam shapes can be described by the following equation:

$$F(\circ) = F_p \times \exp(-2 \times (r/\omega_0)^n) \quad (1)$$

where $F(\circ)$ is the round fluence distribution in the ablation spot, while r denotes the radial distance, and n represents the order of the super-Gaussian probability density function. The focused beam can be defined as the distance from the center of the ablation spot to the edge, where the fluence is equal to $1/e^2$ times the peak fluence F_p and it is defined by the beam waist, ω_0, a fundamental parameter that characterizes the beam width. It's a constant for a given beam setup, and the smaller the ω_0, the more tightly focused the beam is [44].

The maximum ablation depth D_{max} per shot increases logarithmically with the F_p, as it is illustrated with the following equation:

$$D_{max} = (1/\alpha) \times \ln(F_p/F_{th}) \quad (2)$$

where F_{th} represents a certain threshold fluence and α is the spectral absorption coefficient.

As previously mentioned, smaller beam profiles, characterized by their sloped edges rather than a flat-top geometry, can lead to significant undersampling, resulting in a rough surface topography. To mitigate this issue, the idea is to pack the ablation spots closer together – to oversample them. An optimal grid contraction is indicated by reduced surface roughness after ablation. For effective surface sampling to a specific depth, it is crucial to carefully control the contraction to ensure a smooth post-ablation surface across all depth layers.

The ablation grid coordinates or ablation craters are determined by a horizontal and vertical contraction factor (k). The coordinates of an orthogonal ablation grid are provided:

$$BS(\circ) \times k_x \times p, BS(\circ) \times k_y \times q \quad (3)$$

where p and q are positive integers associated with laser spot indexing in the ablation matrix [35].

For the closest packing of the square flat-top crater profiles (where n $= \infty$), the contraction factor is $k = 1$. In contrast, super-Gaussian crater profiles (where n $< \infty$) have a contraction factor of $k < 1$.

By symmetrically contracting the ablation grids ($k_x = k_y$) to match the crater geometry, the optimal contraction factor can be identified.

However, determining this requires knowledge of the super-Gaussian order (n). We achieved this by using our script to analyze ablation craters of various sizes using two different laser ablation systems. The value of n determines how flat-topped or steep-edged the beam profile is. If $n = 2$, it is a classical Gaussian beam, while for $n > 2$, the beam becomes a super-Gaussian, approaching the flat-top shape the higher the values, as can be seen in Fig. 1.

We used gelatin standards to ablate craters of different diameters. The selected ones were 5 μm, 10 μm, 15 μm, 20 μm, and 25 μm for the 193 nm laser ablation system, as well as 10 μm, 15 μm, 20 μm, and 25 μm for the 213 nm laser ablation system. The dosage used was $D = 1$, a single laser shot that allowed for exploring the geometry of the craters. For the mentioned beam diameters and laser systems, the used fluences were 0.5 J cm^{-2}, 1.0 J cm^{-2}, 2.0 J cm^{-2}, 3.0 J cm^{-2}, and 4.0 J cm^{-2}. For all the beam size and fluence combinations, 25 replicate measurements were performed. The ablated samples were then subjected to profilometer measurements, allowing for examination of the sample surfaces. The collected data was imported into the custom-made script that allowed us to extract the super-Gaussian order (n) and volume (V).

Fig. 2 shows the effect of different beam sizes and laser fluences on the super-Gaussian order (n) of the craters for two different laser ablation systems operating at 193 nm (Fig. 2A) and 213 nm (Fig. 2B). The super-Gaussian order characterizes the beam profile, with higher values indicating a more flat-top shape. In general, an increase in beam size leads to an increase in n, indicating a transition to a more uniform (flat-top) crater profile at larger beam sizes. However, the absolute values of n and the rate of increase across the beam sizes differ significantly between the two systems.

For the 193 nm laser, all crater sizes exhibit super-Gaussian properties, with the smallest beam size (BS = 5 μm) approaching a Gaussian profile at certain fluences. In contrast, beam sizes below 10 μm were excluded from the analysis for the 213 nm laser due to poorly defined craters, making it difficult to accurately determine the value of n. In addition, the super-Gaussian order values for the 213 nm system are significantly lower than those obtained with the 193 nm laser, which is illustrated by the different scales of the y-axis. The variation in n across the beam sizes is also less pronounced for the 213 nm laser, indicating that the measured craters are more similar in geometry and tend to lean toward a Gaussian profile.

In terms of fluence, for the 193 nm system (Fig. 2A), higher fluences (2–4 J cm^{-2}) generally lead to a more pronounced increase in n, especially for beam sizes ≥15 μm. This indicates that higher fluences contribute to a more homogeneous beam profile. Interestingly, using the lowest fluence (0.5 J cm^{-2}) with this laser system results in craters with a more pronounced super-Gaussian nature compared to those produced at higher fluences. At higher fluences, excessive heating can cause surface melting in addition to ablation, leading to the formation of an almost perfect Gaussian crater shape ($n \approx 2$) and contributing to fractionation (see Supplementary Material, SI-1). Therefore, the non-monotonic behavior of the super-Gaussian order with fluence could be due to competing effects such as changes in ablation efficiency, material response to laser energy, or interaction dynamics between the beam and the material.

In contrast, the 213 nm system (Fig. 2B) shows a much weaker dependence of n on fluence, except for beam sizes of 10 μm and 25 μm. At 25 μm, the lowest fluence (0.5 J cm^{-2}) leads to the highest n and thus deviates from the trend observed in the 193 nm system. However, it is worth noting that the measurements at 0.5 J cm^{-2} on the 213 nm system also show significantly higher standard deviations compared to other fluence values, indicating greater variability and lower reliability.

These results highlight the differences in the way the two laser systems interact with the material, with the 193 nm system producing more distinct super-Gaussian profiles and being more sensitive to fluence fluctuations than the 213 nm system.

This can pose a major challenge during mapping, as different crater geometries have a considerable influence on the volume ablated during laser ablation (see Fig. 3). The square crater with a flat top (A) represents an ideal case where the entire area is ablated evenly, resulting in 100 % volume coverage. In contrast, an ideal round crater with the same diameter (B) occupies only 78.54 % of the volume, as a round beam does not fully utilize the square mapping grid and leaves gaps. The situation becomes even more complex with a Gaussian crater (C), where a super-Gaussian order of $n = 2$ leads to a crater volume that is only 24.03 % of the theoretical flat crater volume. This smaller volume is due to the Gaussian energy distribution, where the highest ablation occurs in the center, while the edges taper off, resulting in a steep-walled geometry.

The significant reduction in ablated volume in Gaussian profiles leads to undersampling as the laser does not fully ablate the material at the edges of each crater. As the laser moves across a sample, neighboring craters partially overlap, and with a Gaussian beam, the incomplete ablation at the edges results in inaccurate material removal. This distortion affects data acquisition as each laser spot is treated as a discrete sampling unit or pixel. If the craters do not represent the entire intended volume, the resulting data may misrepresent the true composition of the material, resulting in an unrealistic pixel representation and spatial inaccuracies in the mapped region. The problem is particularly critical when small beam sizes are used, where the proportion of material removed per pulse is even smaller, exacerbating the effect of undersampling.

Overall, Fig. 3 underlines the importance of the choice of beam profile for reliable laser ablation mapping. A flat beam profile provides the most efficient and uniform material ablation, while a Gaussian profile results in significant volume loss and lower scanning accuracy.

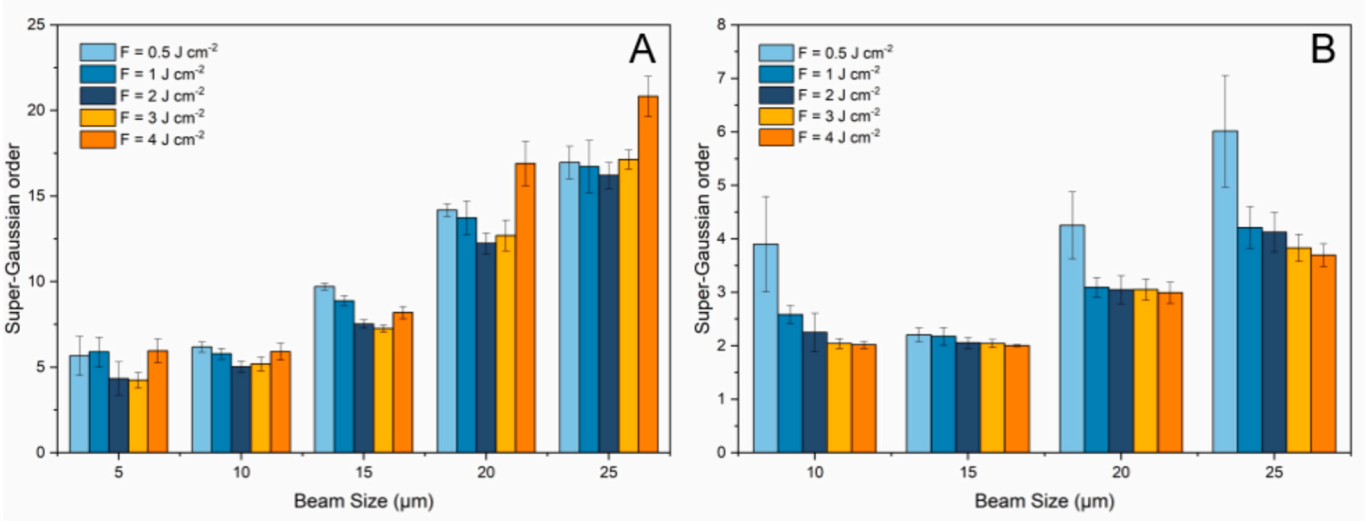

Fig. 2. Influence of varying laser beam sizes (BS) and fluences (F) on the super-Gaussian order (n) for the 193 nm laser ablation system (A) and the 213 nm laser ablation system (B).

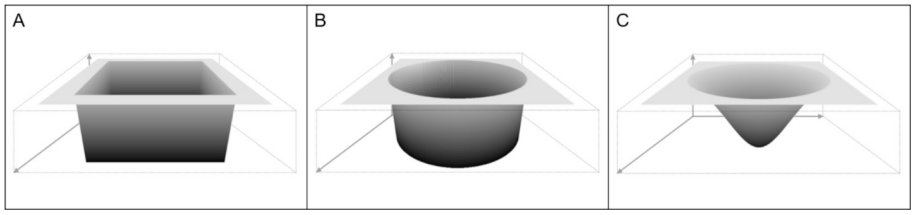

Fig. 3. 3D models illustrating a volume occupied by a flat-topped square crater, 100 % (A), an ideal round crater of the same diameter, 78.54 % (B), and a Gaussian crater with the super-Gaussian order $n = 2$, 24.03 % (C).

To enhance mapping accuracy, optimizing the beam profile by increasing the super-Gaussian order or applying beam shaping techniques can help mitigate these effects and ensure more accurate data representation.

The geometry of the laser beam plays a critical role in determining the accuracy of sampling and mapping processes, as illustrated in Fig. 4. This figure visually demonstrates the effect of different beam profiles on sampling accuracy and data representation in laser ablation mapping.

The simulated ablation profiles were derived assuming that the sample concentrations exhibit a uniform depth profile. The original image (Fig. 4A) serves as a reference and shows an idealized pattern. However, as beam profiles change, distortions in sampling become apparent. The square beam (Fig. 4B) appears pixelated and less defined at smaller scales, illustrating how the ideal shape is compromised by reduced area coverage. The round beam (Fig. 4C) also shows pixelation, with clear gaps between adjacent ablated areas. The difference between the square and round beam profiles (Fig. 4E) emphasizes these inconsistencies and highlights how changes in beam shape affect material removal.

The Gaussian beam brings additional challenges, as can be seen in Fig. 4D and F. The Gaussian profile results in uneven ablation with edges that are faded rather than sharply defined. The difference image between the square and Gaussian beam profiles illustrates how Gaussian beams lead to undersampling, where large parts of the original pattern are poorly represented. To better illustrate those relative differences between beam profiles, Fig. 4E and F were normalized to their shared maximum value, rather than individually scaled from 0 to 1 as in the preceding panels.

The undersampling effect becomes even more problematic when small beam sizes are used, as the reduced energy distribution does not ablate the material evenly across the mapping area.

This emphasizes the importance of beam geometry in laser ablation mapping. Rounding of beam profiles, especially at smaller scales, leads to gaps and incomplete data collection, which ultimately affects mapping accuracy. The transition from a sharp-edged square profile to a more diffuse Gaussian profile leads to considerable undersampling, further underscoring the importance of optimizing both beam shape and fluence to ensure accurate and reliable data acquisition for precise laser mapping applications.

In addition to quantifying the super-Gaussian order, the volumes of the craters were also assessed (Fig. 5). The 193 nm system (A) shows an almost linear trend, where an increase in beam size leads to a proportional increase in ablated volume, supporting the trends observed in our previous studies [45]. This system also exhibits high reproducibility, as evidenced by the minimal experimental uncertainties and the absence of visible error bars. The consistency of the crater volumes indicates a stable ablation process, which underlines the reliability of this laser system for applications requiring precise material ablation.

In contrast, the 213 nm system (B) exhibits a significantly higher measurement variability, as shown by the large relative standard deviation (RSD). The greater uncertainty in the measurement of the crater volume indicates inconsistencies in the ablation process, leading to highly variable and non-reproducible craters. This variability correlates with the previously discussed differences in the super-Gaussian order (Fig. 2), where the 213 nm system produced craters with lower super-Gaussian values, implying a less uniform beam profile. The irregular crater formation not only affects ablated volume consistency but also the accuracy of spatial mapping and bulk concentration analysis, as it undermines the reliability of the results.

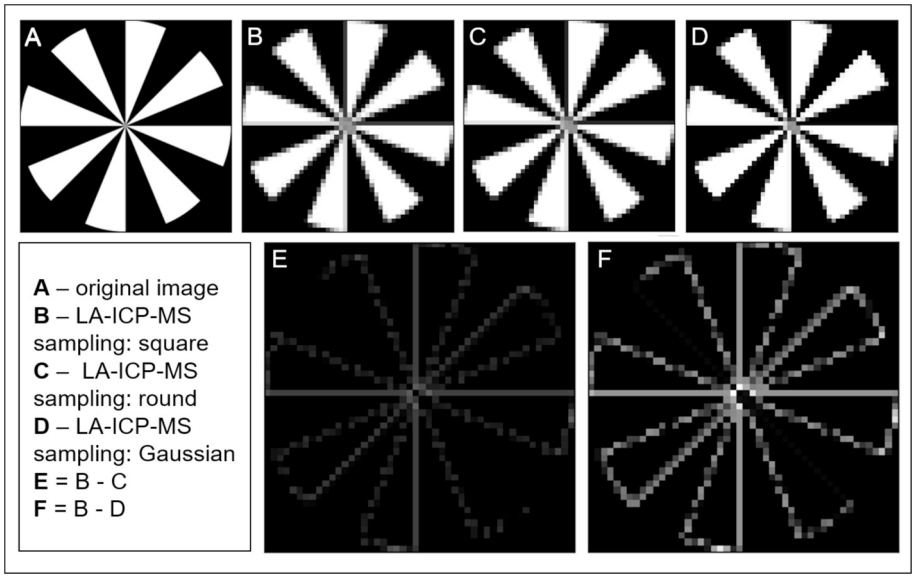

Fig. 4. Visual representation of the mapping of a computed sample (A) using different laser beam profiles: square (B), round (C), and Gaussian (D). The differences between these profiles are highlighted in (E) and (F), showcasing the variations in sampling accuracy and beam-induced distortions.

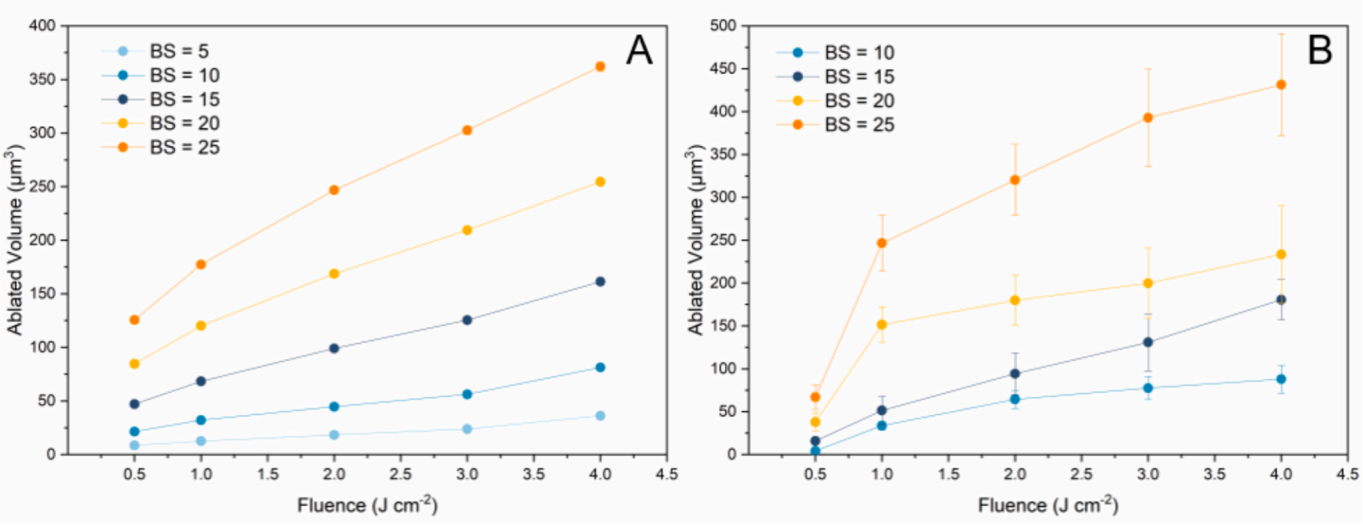

Fig. 5. The relationship between fluence and ablated volume for different beam sizes (BS) for the 193 nm ns laser ablation system (A) and the 213 nm ns laser ablation system (B).

4. Conclusions

The geometric characteristics of laser ablation craters are quite complex. Even though LA-ICP-MS instruments are homogenized to achieve a flat-top shape for ideal surface sampling, the actual crater morphology follows symmetric probability density functions with elevated super-Gaussian orders (n). For the lower values of n, these profiles approximate Gaussian distributions, particularly evident in smaller beam sizes where round beam profiles dominate LA-ICP-MS applications. Notably, even square beam profiles naturally approach a rounded shape as beam sizes decrease. There is a significant challenge in surface sampling to improve the signal-to-noise ratio. To address this limitation, an oversampling approach has emerged as an effective solution, requiring a careful balance between image noise and image blur. To do so, it is important to determine the appropriate contraction of the ablation grid, which can be derived from the super-Gaussian order. Our research provides an elegant way to yield the parameter n, allowing for determining the exact contraction factor (k). Our findings also demonstrate that laser wavelength and beam size selection critically influence crater morphology, directly impacting sampling efficiency. Through the strategic application of oversampling and adjustment of the contraction factor based on the super-Gaussian order, it is possible to achieve enhanced lateral and depth resolution, resulting in smoother post-ablation surfaces. These advancements in understanding and controlling crater geometry represent a significant step forward in optimizing LA-ICP-MS methodologies.

CRediT authorship contribution statement

Antea Hrepić: Writing – review & editing, Writing – original draft, Visualization, Software, Investigation, Formal analysis, Data curation, Conceptualization. **Filip Cernatić:** Writing – review & editing, Software, Formal analysis, Data curation. **Kristina Mervič:** Writing – review & editing, Supervision, Formal analysis. **Sanda Rončević:** Writing – review & editing, Funding acquisition. **Ivan Nemet:** Writing – review & editing, Supervision. **Martin Šala:** Writing – review & editing, Supervision, Resources, Methodology, Funding acquisition.

Author statement

The authors declare that this work is original, has not been published elsewhere, and is not currently under consideration by another journal. No conflicts of interest exist. The authors have made significant contributions to the research and manuscript preparation.

Declaration of competing interest

The authors declare no competing financial interest.

Acknowledgments

The authors acknowledge the financial support from the Slovenian Research and inovation Agency (ARIS), research core funding No. P1-0034 and No. P2-0152. A.H. thanks ARIS for funding her PhD research (researcher's ARIS number: 56955). This research was also performed using resources from the Laboratory of Analytical Atomic Spectrometry, Faculty of Science, University of Zagreb, funded by the European Regional Development Fund (infrastructural project CIuK, grant number KK.01.1.1.02.0016).

The authors would like to thank their former colleagues, Johannes van Elteren and Dino Metarapi, for their valuable contributions to the initial conceptual development of this work.

Appendix A. Supplementary data

Supplementary data to this article can be found online at https://doi.org/10.1016/j.sab.2025.107305.

Data availability

Data will be made available on request.

References

[1] P.A. Doble, R.G. de Vega, D.P. Bishop, D.J. Hare, D. Clases, Laser ablation–inductively coupled plasma–mass spectrometry imaging in biology, Chem. Rev. 121 (19) (2021) 11769–11822, https://doi.org/10.1021/acs.chemrev.0c01219.

[2] J. Liu, L. Zheng, X. Wei, B. Wang, H. Chen, M. Chen, M. Wang, W. Feng, J. Wang, Quantitative imaging of trace elements in brain sections of Alzheimer's disease mice with laser ablation inductively coupled plasma-mass spectrometry, Microchem. J. 172 (2022) 106912, https://doi.org/10.1016/j.microc.2021.106912.

[3] R. Corzo, T. Hoffman, P. Weis, J. Franco-Pedroso, D. Ramos, J. Almirall, The use of LA-ICP-MS databases to calculate likelihood ratios for the forensic analysis of glass evidence, Talanta 186 (2018) 655–661, https://doi.org/10.1016/j.talanta.2018.02.027.

[4] T. Vaculovič, K. Breiter, Z. Korbelová, N. Venclová, K. Tomková, Š. Jonášová, V. Kanický, Quantification of elemental mapping of heterogeneous geological sample by laser ablation inductively coupled plasma mass spectrometry,

Microchem. J. 133 (2017) 200–207, https://doi.org/10.1016/j.microc.2017.03.040.
[5] A.L. Gray, Solid sample introduction by laser ablation for inductively coupled plasma source mass spectrometry, Analyst 110 (5) (1985) 551, https://doi.org/10.1039/an9851000551.
[6] M.B. Fricker, D. Günther, Instrumentation, fundamentals, and application of laser ablation-inductively coupled plasma-mass spectrometry, in: Natural Science in Archaeology, 2016, pp. 1–19, https://doi.org/10.1007/978-3-662-49894-1_1.
[7] R. Hergenröder, O. Samek, V. Hommes, Femtosecond laser ablation elemental mass spectrometry, Mass Spectrom. Rev. 25 (4) (2006) 551–572, https://doi.org/10.1002/mas.20077.
[8] H. Hébert, F. Vidal, F. Martin, J.C. Kieffer, A. Nadeau, T.W. Johnston, A. Blouin, A. Moreau, J.P. Monchalin, Ultrasound generated by a femtosecond and a picosecond laser pulse near the ablation threshold, J. Appl. Phys. 98 (3) (2005), https://doi.org/10.1063/1.1999827.
[9] F. Poitrasson, F.-X. d'Abzac, Femtosecond laser ablation inductively coupled plasma source mass spectrometry for elemental and isotopic analysis: are ultrafast lasers worthwhile? J. Anal. At. Spectrom. 32 (6) (2017) 1075–1091, https://doi.org/10.1039/c7ja00084g.
[10] D. von der Linde, K. Sokolowski-Tinten, J. Bialkowski, Laser–solid interaction in the femtosecond time regime, Appl. Surf. Sci. 109-110 (1997) 1–10, https://doi.org/10.1016/s0169-4332(96)00611-3.
[11] V. Margetic, A. Pakulev, A. Stockhaus, M. Bolshov, K. Niemax, R. Hergenröder, A comparison of nanosecond and femtosecond laser-induced plasma spectroscopy of brass samples, Spectrochim. Acta B At. Spectrosc. 55 (2000) 1771–1785, https://doi.org/10.1016/s0584-8547(00)00275-5.
[12] K. Zong, J. Chen, Z. Hu, Y. Liu, M. Li, H. Fan, Y. Meng, In-situ U-Pb dating of uraninite by fs-LA-ICP-MS, Sci. China Earth Sci. 58 (10) (2015) 1731–1740, https://doi.org/10.1007/s11430-015-5154-y.
[13] C. Pécheyran, S. Cany, O. Donard, Femtosecond laser ablation operating at high repetition rate and low energy coupled in an ICPMS detection: preliminary results, Can. J. Anal. Sci. Spectrosc. 50 (2005) 228–239.
[14] M. Ohata, D. Tabersky, R. Glaus, J. Koch, B. Hattendorf, D. Günther, Comparison of 795 nm and 265 nm femtosecond and 193 nm nanosecond laser ablation inductively coupled plasma mass spectrometry for the quantitative multi-element analysis of glass materials, J. Anal. At. Spectrom. 29 (8) (2014) 1345, https://doi.org/10.1039/c4ja00030g.
[15] M. Ohata, N. Nonose, L. Dorta, D. Günther, Comparison of 265 nm femtosecond and 213 nm nanosecond laser ablation inductively coupled plasma mass spectrometry for Pb isotope ratio measurements, Anal. Sci. 31 (12) (2015) 1309–1315, https://doi.org/10.2116/analsci.31.1309.
[16] X.-Y. Zheng, B.L. Beard, S. Lee, T.R. Reddy, H. Xu, C.M. Johnson, Contrasting particle size distributions and Fe isotope fractionations during nanosecond and femtosecond laser ablation of Fe minerals: implications for LA-MC-ICP-MS analysis of stable isotopes, Chem. Geol. 450 (2017) 235–247, https://doi.org/10.1016/j.chemgeo.2016.12.038.
[17] T.E. Jeffries, W.T. Perkins, N.J.G. Pearce, Comparisons of infrared and ultraviolet laser probe microanalysis inductively coupled plasma mass spectrometry in mineral analysis, Analyst 120 (5) (1995) 1365, https://doi.org/10.1039/an9952001365.
[18] T.E. Jeffries, N.J.G. Pearce, W.T. Perkins, A. Raith, Chemical fractionation during infrared and ultraviolet laser ablation inductively coupled plasma mass spectrometry—implications for mineral microanalysis, Anal. Commun. 33 (1) (1996) 35–39, https://doi.org/10.1039/ac9963300035.
[19] C. Geertsen, A. Briand, F. Chartier, J.-L. Lacour, P. Mauchien, S. Sjöström, J.-M. Mermet, Comparison between infrared and ultraviolet laser ablation at atmospheric pressure—implications for solid sampling inductively coupled plasma spectrometry, J. Anal. At. Spectrom. 9 (1) (1994) 17–22, https://doi.org/10.1039/ja9940900017.
[20] D. Figg, M.S. Kahr, Elemental fractionation of glass using laser ablation inductively coupled plasma mass spectrometry, Appl. Spectrosc. 51 (8) (1997) 1185–1192, https://doi.org/10.1366/0003702971941728.
[21] M. Guillong, I. Horn, D. Günther, A comparison of 266 nm, 213 nm and 193 nm produced from a single solid state Nd:YAG laser for laser ablation ICP-MS, J. Anal. At. Spectrom. 18 (10) (2003) 1224–1230, https://doi.org/10.1039/b305434a.
[22] J. Gonzalez, X.L. Mao, J. Roy, S.S. Mao, R.E. Russo, Comparison of 193, 213 and 266 nm laser ablation ICP-MS, J. Anal. At. Spectrom. 17 (9) (2002) 1108–1113, https://doi.org/10.1039/b202122f.
[23] T. Jeffries, S.E. Jackson, H.P. Longerich, Application of a frequency quintupled Nd:YAG source (λ=213 nm) for laser ablation inductively coupled plasma mass spectrometric analysis of minerals, J. Anal. At. Spectrom. 13 (9) (1998) 935–940, https://doi.org/10.1039/a801328d.
[24] G.H. Pettit, M.N. Ediger, Corneal-tissue absorption coefficients for 193- and 213-nm ultraviolet radiation, Appl. Opt. 35 (19) (1996) 3386, https://doi.org/10.1364/ao.35.003386.
[25] V.M. Neves, G.M. Heidrich, E.S. Rodrigues, M.S.P. Enders, E.I. Muller, F. T. Nicoloso, HwPd Carvalho, V.L. Dressler, La2O3 nanoparticles: study of uptake and distribution in Pfaffia glomerata (Spreng.) Pedersen by LA-ICP-MS and μ-XRF, Environ. Sci. Technol. 53 (18) (2019) 10827–10834, https://doi.org/10.1021/acs.est.9b02868.
[26] T. Ubide, C.A. McKenna, D.M. Chew, B.S. Kamber, High-resolution LA-ICP-MS trace element mapping of igneous minerals: in search of magma histories, Chem. Geol. 409 (2015) 157–168, https://doi.org/10.1016/j.chemgeo.2015.05.020.
[27] Q. Li, Y. Fang, J. Liu, C. Zhang, Z. Wang, Elemental imaging of alumina ceramic tube using laser ablation-inductively coupled plasma-mass spectrometry (LA-ICP-MS), At. Spectrosc. 42 (3) (2021) 154–159.
[28] T. Van Acker, S.J.M. Van Malderen, T. Van Helden, C. Stremtan, M. Šala, J.T. van Elteren, F. Vanhaecke, Analytical figures of merit of a low-dispersion aerosol transport system for high-throughput LA-ICP-MS analysis, J. Anal. At. Spectrom. 36 (6) (2021) 1201–1209, https://doi.org/10.1039/D1JA00110H.
[29] S.J.M. Van Malderen, A.J. Managh, B.L. Sharp, F. Vanhaecke, Recent developments in the design of rapid response cells for laser ablation-inductively coupled plasma-mass spectrometry and their impact on bioimaging applications, J. Anal. At. Spectrom. 31 (2) (2016) 423–439, https://doi.org/10.1039/c5ja00430f.
[30] D.N. Douglas, A.J. Managh, H.J. Reid, B.L. Sharp, High-speed, integrated ablation cell and dual concentric injector plasma torch for laser ablation-inductively coupled plasma mass spectrometry, Anal. Chem. 87 (22) (2015) 11285–11294, https://doi.org/10.1021/acs.analchem.5b02466.
[31] J.T. van Elteren, V.S. Šelih, M. Šala, Insights into the selection of 2D LA-ICP-MS (multi)elemental mapping conditions, J. Anal. At. Spectrom. 34 (9) (2019) 1919–1931, https://doi.org/10.1039/c9ja00166b.
[32] M. Šala, V.S. Šelih, C.C. Stremtan, T. Tămaş, J.T. van Elteren, Implications of laser shot dosage on image quality in LA-ICP-QMS imaging, J. Anal. At. Spectrom. 36 (1) (2021) 75–79, https://doi.org/10.1039/d0ja00381f.
[33] D. Metarapi, J.T. van Elteren, High-resolution single pulse LA-ICP-MS mapping via 2D sub-pixel oversampling on orthogonal and hexagonal ablation grids – a computational assessment, Talanta 263 (2023) 124699, https://doi.org/10.1016/j.talanta.2023.124699.
[34] J.T. van Elteren, M. Šala, D. Metarapi, Comparison of single pulse, multiple dosage, and 2D oversampling / deconvolution LA-ICPMS strategies for mapping of (ultra) low-concentration samples, Talanta 235 (2021) 122785, https://doi.org/10.1016/j.talanta.2021.122785.
[35] J.T. van Elteren, D. Metarapi, K. Mervič, M. Šala, Exploring the benefits of ablation grid adaptation in 2D/3D laser ablation inductively coupled plasma mass spectrometry mapping through geometrical modeling, Anal. Chem. 95 (26) (2023) 9863–9871, https://doi.org/10.1021/acs.analchem.3c00774.
[36] K. Gillen-Christandl, G.D. Gillen, M.J. Piotrowicz, M. Saffman, Comparison of Gaussian and super Gaussian laser beams for addressing atomic qubits, Appl. Phys. B Lasers Opt. 122 (5) (2016), https://doi.org/10.1007/s00340-016-6407-y.
[37] S.J.M. Van Malderen, J.T. van Elteren, F. Vanhaecke, Submicrometer imaging by laser ablation-inductively coupled plasma mass spectrometry via signal and image deconvolution approaches, Anal. Chem. 87 (12) (2015) 6125–6132, https://doi.org/10.1021/acs.analchem.5b00700.
[38] S. Verma, S. Maheshwari, R. Singh, P. Chaudhari, Laser in dentistry: an innovative tool in modern dental practice, Natl. J. Maxillofac. Surg. 3 (2) (2012) 124, https://doi.org/10.4103/0975-5950.111342.
[39] B.Z. Balázs, N. Geier, M. Takács, J.P. Davim, A review on micro-milling: recent advances and future trends, Int. J. Adv. Manuf. Technol. 112 (3–4) (2020) 655–684, https://doi.org/10.1007/s00170-020-06445-w.
[40] T.-I. Kim, J.L. Alió del Barrio, M. Wilkins, B. Cochener, M. Ang, Refractive surgery, Lancet 393 (10185) (2019) 2085–2098, https://doi.org/10.1016/s0140-6736(18)33209-4.
[41] S. Verma, J. Hesser, S. Arba-Mosquera, Optimum laser beam characteristics for achieving smoother ablations in laser vision correction, Invest. Opthalmol. Vis. Sci. 58 (4) (2017) 2021, https://doi.org/10.1167/iovs.16-21025.
[42] L. St-Onge, A mathematical framework for modeling the compositional depth profiles obtained by pulsed laser ablation, J. Anal. At. Spectrom. 17 (9) (2002) 1083–1089, https://doi.org/10.1039/b203024c.
[43] M. Šala, V.S. Šelih, J.T. van Elteren, Gelatin gels as multi-element calibration standards in LA-ICP-MS bioimaging: fabrication of homogeneous standards and microhomogeneity testing, Analyst 142 (18) (2017) 3356–3359, https://doi.org/10.1039/c7an01361b.
[44] S.D. Silvestri, P. Laporta, V. Magni, O. Svelto, Solid-state laser unstable resonators with tapered reflectivity mirrors: the super-Gaussian approach, IEEE J. Quantum Electron. 24 (6) (1988) 1172–1177, https://doi.org/10.1109/3.240.
[45] A. Jerše, K. Mervič, J.T. van Elteren, V.S. Šelih, M. Šala, Quantification anomalies in single pulse LA-ICP-MS analysis associated with laser fluence and beam size, Analyst 147 (23) (2022) 5293–5299, https://doi.org/10.1039/D2AN01172G.